Flow, Turbulence, and Combustion manuscript No.
(will be inserted by the editor)

Assessing Stretched-Vortex Subgrid-Scale Models in Finite Volume Methods for Unbounded Turbulent Flows

Sean Walters · Xinfeng Gao · Hans Johansen · Stephen Guzik

Received: date / Accepted: date

Abstract Large-eddy simulation provides a feasible route to solutions of higher physical fidelity than those offered by Reynolds-averaged Navier-Stokes simulations while avoiding the intractable computational expense of direct numerical simulations. While implicit large-eddy simulations have seen widespread use for high-speed turbulent flows, it is unclear how the underlying stability techniques of the computational algorithms interact with added explicit turbulence models. Specific questions include whether the former can substitute for the latter (implicit large-eddy simulation), whether the latter can by itself regularize an infinite-Reynolds number calculation, and the effect of simultaneously using both. In the context of a fourth-order finite-volume method, this study investigates the inter-

This research was supported by Department of Defense United States Air Force (DOD-USAF-Air Force) under the award number FA9550-18-1-0057. This material is partly based upon work at Lawrence Berkeley National Laboratory (LBNL) supported by the U.S. Department of Energy, Office of Science, Advanced Scientific Computing Research, under contract number DE-AC02-05CH11231. This research was supported by the National Science Foundation under the award number 1723191.

S. Walters
Computational Fluid Dynamics and Propulsion Laboratory, Colorado State University, Fort Collins, CO 80523, USA

X. Gao
Computational Fluid Dynamics and Propulsion Laboratory, Colorado State University, Fort Collins, CO 80523, USA

H. Johansen
Applied Numerical Algorithms Group, Lawrence Berkeley National Laboratory, Berkeley, CA 94720, USA

S. Guzik
Computational Fluid Dynamics and Propulsion Laboratory, Colorado State University, Fort Collins, CO 80523, USA
Tel.: 970-491-4682
Fax: 970-491-3827
E-mail: Stephen.Guzik@colostate.edu

action between the stretched-vortex large-eddy simulation model and both the piecewise parabolic method for limiting and fifth-order upwinding (or hyperviscosity). The stretched-vortex model is shown to simulate the Taylor-Green vortex and a double-shear-layer in a more satisfactory manner than implicit large-eddy simulations. Furthermore, the limiter and the fifth-order interpolation alter the flow field in an undesirable manner even when the explicit turbulence model is utilized.

Keywords High-Order Finite Volume Methods · Large Eddy Simulation · Stretched-Vortex Turbulence Model · High Reynolds Number Flows

1 Introduction

Many flows of engineering interest are turbulent and inherently multiscale. Numerically resolving all scales in a high Reynolds number turbulent flow is challenging with today's computational capabilities. However, large-eddy simulation (LES) is a promising alternative to direct numerical simulations (DNS) in that it solves large scales but models small scale effects to provide a solution accuracy acceptable for many engineering requirements. The approach is logical when rate-limiting processes happen at the larger resolved scales [**?**]. Even so, defining and modeling the small scales becomes one of the key issues in LES.

The typical LES definition of small scales begins with the separation of the fully resolved solution field, ϕ, into scales representable by the LES, $\bar{\phi}$, and scales which are unrepresentable, ϕ'. To perform this separation, a standard LES low-pass filter operator, the convolution operator, convolves the original field with an explicitly or implicitly defined filter kernel, G,

$$G \star \phi = \bar{\phi}\left(\mathbf{x}, t\right) = \int_{-\infty}^{\infty} \int_{-\infty}^{\infty} \phi\left(\boldsymbol{\xi}, \tau\right) G\left(\mathbf{x} - \boldsymbol{\xi}, t - \tau\right) d\tau d\boldsymbol{\xi} \ , \tag{1}$$

where $\mathbf{x}$ and t are space and time respectively. While this filter is almost universally applied to equations describing LES simulations, explicit definition of the filter is rare. Rather, an implicit filter arises from the combined effects of the discretization, the numerical scheme, and any subgrid-scale (SGS) models used. This study utilizes an implicitly defined Favre-averaged filter where velocity is defined as mass-weighted momentum, $\tilde{\mathbf{u}} = \overline{\rho \mathbf{u}}/\bar{\rho}$.

After applying a filter, all unknown quantities must be modeled using known quantities. Suppose the time advancement of $\bar{\phi}$ and $\bar{\psi}$ requires $\overline{\phi\psi}$ which is not automatically evolved in time. A model for $\overline{\phi\psi}$ in terms of $\bar{\phi}$ and $\bar{\psi}$ is then required. Explicitly modeled LES incorporates models developed for these filtered nonlinear terms, while implicit LES (ILES) relies on characteristics of the numerical algorithm to provide the necessary modeling.

In recent decades, the LES field has seen increasing application of ILES to complex flows of engineering interest [18]. As increasingly complex physics is simulated, the potential for stabilized finite-volume methods (FVMs) to accurately predict widely varying phenomenon is broadly appealing. Some of the these ILES methods are based on discrete approximations of forward and inverse explicit LES filters, closely mimicking generalized, high-order extensions of FVMs, which are similar to early explicit LES models [12, 15, 6, 21]. If ILES schemes are sufficient to

accurately predict the evolution of high Reynolds number turbulent flows, explicit turbulence models could be dispensed with at the benefit of computational cost. Moreover, one could solve flows featuring discontinuities without worrying about interactions of the turbulence model with limiters. At the very worst in terms of computational expense, an explicit turbulence model could augment the stabilization features of the FVM if the explicit model is necessary to simulate the correct evolution of the turbulent flow. This study utilizes the stretched vortex (SV) SGS model to close the filtered governing equations. This structural model has been shown to provide results that are consistent with experimental data for Reynolds number as high as $\approx 10^6$. Additionally, extensions to scalar transport, variable density flows, and compressible flows are natural for the SV model. For this reason, this structural LES model is used throughout this study. The system is simulated with a high-order FVM which is optionally stabilized using the piecewise parabolic method (PPM) or the inherent upwinding of fifth-order face-interpolations.

The goal of the present study is to investigate the necessity of using the stretched-vortex model in the context of high Reynolds number, unbounded turbulent flows. The FVM algorithm being utilized has been specifically designed for high-speed, reacting, turbulent flows and will necessarily require strong stabilization mechanisms in future simulations of these cases. Steep solution gradients and even discontinuities such as shocks are present in unresolved, high Reynolds number turbulence and in high-speed, reacting, turbulent flows. When solving these flow features, some form of strong stabilization, such as a limiter, is required. Naturally, the impact of the limiter on the LES solution accuracy must be investigated. Study of the stabilization mechanisms in flows where a rather simple dissipation mechanism would suffice is useful to provide recommendations for future use when strong stabilization mechanisms are no longer optional. If an ILES algorithm using the PPM scheme or fifth-order face-interpolation sufficiently simulates fully turbulent, spatially periodic test cases which lack grid-resolved physical viscosity, it is assumed the stretched-vortex model will be unnecessary in cases of high-speed, reacting turbulent flows. If these ILES schemes are insufficient for these test cases, the present study intends to determine whether simply adding the stretched-vortex model is sufficient. In the event that this, too, is insufficient or the stretched-vortex model on its own provides more accurate results, recommendations will be made for further research.

Throughout this study, the equations describing a compressible fluid flow, i.e. the conservation of mass (ρ), momentum ($\rho\mathbf{u}$), and energy (ρe), will be considered. These equations are given as follows:

$$\frac{\partial \rho}{\partial t} + \boldsymbol{\nabla} \cdot (\rho \mathbf{u}) = 0 \ , \tag{2}$$

$$\frac{\partial}{\partial t} (\rho \mathbf{u}) + \boldsymbol{\nabla} \cdot \left(\rho \mathbf{u}\mathbf{u}^\top + \mathbf{I} p \right) = \boldsymbol{\nabla} \cdot \boldsymbol{\tau} \ , \tag{3}$$

$$\frac{\partial}{\partial t} (\rho e) + \boldsymbol{\nabla} \cdot (\rho \mathbf{u} e + \mathbf{u} p) = \boldsymbol{\nabla} \cdot (\boldsymbol{\tau} \cdot \mathbf{u}) - \boldsymbol{\nabla} \cdot \mathbf{q} \ , \tag{4}$$

where $\mathbf{I}$ is the identity matrix. The fluid is assumed to be a Newtonian, calorically perfect, ideal gas and its stress, $\boldsymbol{\tau}$, is modeled by

$$\boldsymbol{\tau} = 2\mu \left(\mathbf{S} - \frac{1}{3} (\boldsymbol{\nabla} \cdot \mathbf{u}) \mathbf{I} \right) \quad , \quad \mathbf{S} = \frac{1}{2} \left(\boldsymbol{\nabla}\mathbf{u} + (\boldsymbol{\nabla}\mathbf{u})^\top \right) \ . \tag{5}$$

Heat flux, $\mathbf{q}$, is approximated by Fourier's law and pressure is computed by,

$$p = (\gamma - 1)\left(\rho e - \frac{1}{2}\rho \mathbf{u}\cdot\mathbf{u}\right) \ . \tag{6}$$

Favre-filtering Eqs. (2 - 4) and Eq. (6) results in

$$\frac{\partial \bar{\rho}}{\partial t} + \boldsymbol{\nabla}\cdot(\bar{\rho}\tilde{\mathbf{u}}) = 0 \ , \tag{7}$$

$$\frac{\partial}{\partial t}(\bar{\rho}\tilde{\mathbf{u}}) + \boldsymbol{\nabla}\cdot\left(\bar{\rho}\widetilde{\mathbf{u}\mathbf{u}^{\top}} + \mathbf{I}\bar{p}\right) = \boldsymbol{\nabla}\cdot\tilde{\boldsymbol{\tau}} \ , \tag{8}$$

$$\frac{\partial}{\partial t}(\bar{\rho}\tilde{e}) + \boldsymbol{\nabla}\cdot(\bar{\rho}\widetilde{\mathbf{u}e} + \widetilde{\mathbf{u}p}) = \boldsymbol{\nabla}\cdot\left(\widetilde{\boldsymbol{\tau}\cdot\mathbf{u}}\right) - \boldsymbol{\nabla}\cdot\tilde{\mathbf{q}} \ , \tag{9}$$

$$\bar{p} = (\gamma - 1)\left(\bar{\rho}\tilde{e} - \frac{1}{2}\bar{\rho}\widetilde{\mathbf{u}\cdot\mathbf{u}}\right) \ . \tag{10}$$

At this point, the filtered equations must be closed by recasting the nonlinear terms as functions of the individually filtered constituents. Even though the equations have been filtered using an unknown, undefined filter and implicit filtering is used throughout this study, it will be assumed that the implicit filter size is approximately equal to the spatial discretization size.

The rest of the paper is organized as follows. Section 2 details the stretched-vortex model and its mathematical form as implemented in the current study. Section 3 describes the high-order FVM algorithm in which the stretched-vortex model is implemented and tested. The test cases and data processing details are presented in Section 4. The results of simulations performed in the current study and discussion regarding the interpretation of these results are presented in Section 5. Finally, Section 6 wraps up the study with conclusions and recommendations for future research.

2 Stretched Vortex Turbulence Model

The stretched-vortex (SV) subgrid-scale (SGS) model, is a structural LES SGS model and is based on the assumption that, at sufficiently high Reynolds numbers and sufficiently small length scales, stretched vortex tubes dominate the flow physics [16,11].

The model closes the filtered momentum equation, Eq. (8), using

$$\left(\widetilde{\mathbf{u}\mathbf{u}^{\top}} - \tilde{\mathbf{u}}\tilde{\mathbf{u}}^{\top}\right) = K\left(\mathbf{I} - \mathbf{e}^{\mathbf{v}}\left(\mathbf{e}^{\mathbf{v}}\right)^{\top}\right) \ , \tag{11}$$

through an approximation of the subgrid kinetic energy, K, and the orientation vector, $\mathbf{e}^{\mathbf{v}}$, of the subgrid vortices.

Requiring K to be positive, it is apparent from the model form that the orientation vector is the only factor determining whether this model is dissipative or anti-dissipative. Many SV SGS papers have utilized an SGS vortex orientation vector depending solely on the strongest eigenvector of the strain-rate tensor, $\mathbf{e}^{\mathbf{v}} = \mathbf{e}^{\mathbf{3}}$, which has been shown to be dissipative [2,13,14]. The present work also utilizes this model in addition to another model originally proposed by Misra

and Pullin ("model 1b"). This model includes the resolved vorticity vector, $\boldsymbol{\omega}$, in addition to the strongest eigenvector of the strain-rate tensor and is formulated as

$$\left(\widetilde{\mathbf{u}\mathbf{u}^{\top}} - \tilde{\mathbf{u}}\tilde{\mathbf{u}}^{\top}\right) = K\left[\sigma\left(\mathbf{I} - \mathbf{e}^{\mathbf{3}}\left(\mathbf{e}^{\mathbf{3}}\right)^{\top}\right) + (1-\sigma)\left(\mathbf{I} - \mathbf{e}^{\boldsymbol{\omega}}\left(\mathbf{e}^{\boldsymbol{\omega}}\right)^{\top}\right)\right] \ , \tag{12}$$

where σ provides a weighting to the two different orientation vectors. Aligning with $\mathbf{e}^{\boldsymbol{\omega}}$ makes the model more anti-dissipative. Throughout the current study, σ is chosen to be 0.5.

Among the various proposed SGS kinetic energy models, [16,20,13,1,2], the model used by Chung and Pullin is consistently applied within this paper [2]. This model,

$$K = \frac{1}{2}\mathcal{K}_0' \Gamma\left(-\frac{1}{3}, \kappa_c^2\right) \ , \tag{13}$$

requires the evaluation of the incomplete gamma function, $\Gamma(\cdot)$, and the grouped Kolmogorov constant, $\mathcal{K}_0'$

$$\mathcal{K}_0' = \frac{[F_2]}{[Q(\kappa_c, d)]} \ . \tag{14}$$

In Eq. (14), $[\cdot]$ is an ensemble average of the variables over a spatial domain, Ω, encompassing N points, $\mathbf{x}_i$, (26 in this study) neighboring $\mathbf{x}_0$

$$[\phi] = \frac{1}{N} \sum_{\mathbf{x}_i \in \Omega \ ; \ \mathbf{x}_i \neq \mathbf{x}_0} \phi(\mathbf{x}_0, \mathbf{x}_i) \ . \tag{15}$$

F_2 is the second-order structure function

$$F_2 = \left(\tilde{\mathbf{u}}(\mathbf{x}_0) - \tilde{\mathbf{u}}(\mathbf{x}_i)\right) \cdot \left(\tilde{\mathbf{u}}(\mathbf{x}_0) - \tilde{\mathbf{u}}(\mathbf{x}_i)\right) \ . \tag{16}$$

Additionally, Q is a scaling parameter dependent on the grid-cutoff size and is given by

$$Q(\kappa_c, d) = 4\int_0^{\kappa_c} \kappa^{-5/3} \exp\left(-\kappa^2\right)\left(1 - J_0(\kappa/\kappa_c)\,\pi d\right) \mathrm{d}\kappa \ , \tag{17}$$

where κ is the wavenumber variable of integration, J_0 is the zeroth-order Bessel function of the first kind, d is the planar distance from the cell center to the SGS vortex axis

$$d = \frac{r}{\Delta_c} \quad , \quad r = \left[(\mathbf{x}_0 - \mathbf{x}_i) \cdot (\mathbf{x}_0 - \mathbf{x}_i)\right]^{1/2} \quad , \quad \Delta_c = (\Delta x \Delta y \Delta z)^{1/3} \ , \tag{18}$$

and κ_c is computed using

$$\kappa_c = \frac{\pi}{\Delta_c}\sqrt{\frac{2\nu}{3|\tilde{a}|}} \quad , \quad \tilde{a} = \left(\mathbf{e}^{\mathbf{v}}\right)^{\top} \tilde{\mathbf{S}} \mathbf{e}^{\mathbf{v}} \quad , \quad \nu = \frac{\mu}{\bar{\rho}} \ . \tag{19}$$

Efficient means of computing $\mathcal{K}_0$, $\Gamma(\cdot)$, and the eigenvalues/eigenvectors are presented by Voelkl and others [20,1,19].

In addition to the closure of the filtered momentum equation, Eq. (8), the current study closes the filtered energy equation, Eq. (9), and the filtered pressure computation, Eq. (10), following the methodology presented by Kosovic, et al. [10] and Hill, et al. [9].

3 Numerical Framework

All results presented in this study are obtained using the high-order finite-volume method (FVM) algorithm, Chord [5,8,7,6,17], which is built upon Chombo [3]. This numerical framework allows the behavior of SGS models to be studied in various flow regimes. Moreover, this study will provide quantitative information on the influence of the algorithm order of accuracy on the SGS model. Specifically, the effects of and differences between fifth-order, fourth-order, and second-order accuracy are examined. Additionally, the SV SGS model is compared to the ILES capabilities already incorporated in Chord in the form of the PPM method. A brief overview of the Chord numerical framework is presented below.

3.1 Chord

Chord is a finite-volume CFD algorithm solving the system of governing equations for transient, compressible, turbulent, reacting and non-reacting fluid flows with complex geometry. It has been designed for achieving superior accuracy and performance for turbulence and combustion simulations on modern high-performance computing architecture. By design, Chord is fourth-order accurate in space and time for smooth flows [5,8,7,6,17]. For flows with strong discontinuities (e.g., shock or detonation waves), the PPM [4,15] limiter is used for stability. Additionally, Chord is capable of second-order and fifth-order face-value interpolations. In time, the solution is evolved using the standard four-stage Runge-Kutta method. Chord is capable of different levels of turbulence modeling, i.e., unsteady Reynolds-averaged Navier-Stokes (URANS), LES, or DNS. Additionally, Chord features adaptive mesh refinement (AMR) in space and subcycling in time, accommodates complex geometry while preserving free-stream conditions using generalized coordinate transformations, and scales to at least 1×10^5 cores.

3.2 Face Interpolation

In FVMs, flux evaluations at the faces of a computational cell are essential and require knowledge of face values. Reconstructing solution variables at cell faces is one of the fundamental operations in the algorithm. The interpolation scheme directly impacts the order of accuracy of the underlying numerical algorithm.

Interpolating the face-averaged primitive state, $\langle \mathbf{W} \rangle_{\boldsymbol{i}+\frac{1}{2}\boldsymbol{e}^d}$, from the cell-averaged primitive state, $\langle \mathbf{W} \rangle_{\boldsymbol{i}}$, follows the process described in previous literature [5,8]. A cell index is denoted by $\boldsymbol{i}$ on an integer lattice and $\boldsymbol{e}^d$ is a unit vector in direction d. A cell face is reached by a shift of 1/2. A four-point, fourth-order, centered approximation to $\langle \mathbf{W} \rangle_{\boldsymbol{i}+\frac{1}{2}\boldsymbol{e}^d}$ is given by

$$\langle \mathbf{W} \rangle_{\boldsymbol{i}+\frac{1}{2}\boldsymbol{e}^d} = \frac{7}{12}\left(\langle \mathbf{W} \rangle_{\boldsymbol{i}} + \langle \mathbf{W} \rangle_{\boldsymbol{i}+\boldsymbol{e}^d}\right) - \frac{1}{12}\left(\langle \mathbf{W} \rangle_{\boldsymbol{i}-\boldsymbol{e}^d} + \langle \mathbf{W} \rangle_{\boldsymbol{i}+2\boldsymbol{e}^d}\right) \ , \tag{20}$$

while the right-biased, five-point, fifth-order approximation is provided by

$$\begin{aligned} \langle \mathbf{W} \rangle_{\boldsymbol{i}+\frac{1}{2}\boldsymbol{e}^d,R} = &\frac{1}{60}\left(-3\langle \mathbf{W} \rangle_{\boldsymbol{i}-\boldsymbol{e}^d} + 27\langle \mathbf{W} \rangle_{\boldsymbol{i}} + 47\langle \mathbf{W} \rangle_{\boldsymbol{i}+\boldsymbol{e}^d} - 13\langle \mathbf{W} \rangle_{\boldsymbol{i}+2\boldsymbol{e}^d}\right) \\ &+ \frac{1}{60}\left(2\langle \mathbf{W} \rangle_{\boldsymbol{i}+3\boldsymbol{e}^d}\right) \ . \end{aligned} \tag{21}$$

A reflection of Eq. (21) about the face provides a left-biased interpolation and the final state on the face is a solution of the Riemann problem. When PPM is not applied, the second-order and fourth-order stencils are centered; the fifth-order stencil adds upwinding which appears as an added hyper-viscosity, dissipating the high-wavenumber content on the grid.

3.3 Numerical Implementation of the SV SGS Model

Within Chord, the SV SGS/SAS model terms are treated as turbulent fluxes and are evaluated at faces in order to maintain conservation of density, momentum, and total energy. The face-centered primitive variables $\mathbf{W}_{\boldsymbol{i}+\frac{1}{2}\boldsymbol{e}^d}$, whether computed using second, fourth, or fifth-order interpolations, are used for the calculation of intertial fluxes, diffusive fluxes, gradients used in the calculation of SV SGS fluxes, and other model terms.

4 Test Cases

Throughout this study, two cases test the concepts and algorithms. The first case uses the Taylor-Green vortex initialization, while the second is a temporally evolving mixing layer.

4.1 Inviscid Taylor-Green Vortex

The Taylor-Green vortex flow is initialized with a sinusoidal initial condition in a triply periodic cube $[0, D]^3$ given by

$$u = -U_0 \sin\left(\frac{n\pi x}{D}\right)\cos\left(\frac{n\pi y}{D}\right)\sin\left(\frac{n\pi z}{D}\right) \tag{22}$$

$$v = U_0 \cos\left(\frac{n\pi x}{D}\right)\sin\left(\frac{n\pi y}{D}\right)\sin\left(\frac{n\pi z}{D}\right) \tag{23}$$

$$w = 0 \tag{24}$$

$$p = p_0 + \frac{\rho_0 U_0^2}{16}\left(\cos\left(\frac{2n\pi x}{D}\right) + \cos\left(\frac{2n\pi y}{D}\right)\right)\left(\cos\left(\frac{2n\pi z}{D}\right) + 2\right) \tag{25}$$

$$\rho = \frac{p}{RT_0} = \frac{p\rho_0}{p_0} \tag{26}$$

where U_0 is the velocity fluctuation magnitude, D is the domain length, and n is the number of vortices contained in the domain in each coordinate direction. The flow has a Mach number of 0.1, and a Prandtl number of 0.71. Cell counts of 128^3 were used for all of the Taylor-Green vortex base-cases. Reference cases for the Taylor-Green vortex were run using 256^3 and 512^3 meshes. More information regarding the choices of computational grids can be found in previous work [21]

In the inviscid limit, the Taylor-Green vortex provides an ideal test of algorithmic components examined in this study, including the underlying FVM order of accuracy, limiters used for numerical stability, and SGS turbulence models. The vortex evolution begins with “vortex wrap-up”, eventually transitioning to a turbulent energy cascade process. It is apparent that all initial kinetic energy

eventually resides at the subgrid-scale even though it is never dissipated in this inviscid problem. Once the kinetic energy resides at the subgrid-scale, it is indistinguishable from internal energy except through a model. As a result, the numerical algorithm must sufficiently dissipate resolved-scale kinetic energy while correctly capturing the energy cascade process. This test case will demonstrate the dissipative characteristics of the algorithms when physical viscosity is absent.

4.2 Time Evolving Mixing Layer

The time evolving mixing-layer considered in the present study is configured as triply periodic double shear as shown in Fig. 1. The air is assumed ideal, with

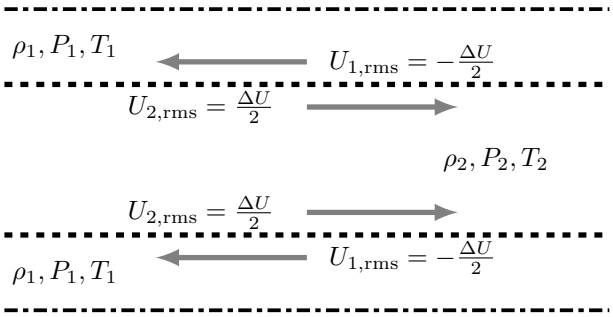

Fig. 1 Configuration of the time-evolving double mixing layers

$\gamma = 1.4$, $Pr = 0.71$, $P_1 = P_2 = 101325\,\mathrm{Pa}$, and $\rho_1 = \rho_2 = 1.225\,\mathrm{kg/m^3}$. The root-mean-square velocities of streams 1 and 2 are $U_{1,\mathrm{rms}} = 34.03\,\mathrm{m/s}$ and $U_{2,\mathrm{rms}} = -U_{1,\mathrm{rms}}$, respectively. The flow has a Mach number, M, of 0.1 based on a velocity equal to the arithmetic mean of the two stream velocities, $U_{1,\mathrm{rms}}$ and $U_{2,\mathrm{rms}}$, and a Reynolds number of 11650, based on

$$Re_{\delta_\omega,0} = \frac{\rho\,|U_{\mathrm{rms}}|\,\delta_\omega}{\mu}\,, \tag{27}$$

where δ_ω is the initial vorticity thickness. The momentum thickness, δ_θ, is $\delta_\omega/4$. The computational domain size is, $L_x \times L_y \times L_z = 137\delta_\theta \times 137\delta_\theta \times 68\delta_\theta$. The meshes consist of fine resolutions with $512 \times 512 \times 256$ cells in the streamwise, shear-layer normal, and spanwise directions respectively and coarse resolutions with $128 \times 128 \times 64$ cells.

The velocities in each stream were sinusoidally perturbed and computed from a stream function in order to achieve an analytically divergence free initial velocity field. This stream function is defined as

$$\Psi = \xi U_{1,\mathrm{rms}} \tanh\left(\frac{\xi}{2\delta_\theta}\right)\,, \tag{28}$$

where the factor ξ is defined as

$$\xi = y + \exp\left(-\eta|y|\right)\left(\sum_i b_i \sin\left(\frac{2\pi\omega_i x}{L} + \phi_i\right)\right) \ , \tag{29}$$

and the velocities are computed analytically as

$$u = \frac{\partial \Psi}{\partial y} \quad , \quad v = -\frac{\partial \Psi}{\partial x} \ . \tag{30}$$

The i-th perturbation mode has phase shift ϕ_i, wavenumber ω_i, and magnitude b_i. The parameter η is a scaling factor to control how quickly the perturbation modes decay in the shear-layer normal direction. For the cases simulated in this study, this scaling factor was chosen as $\eta = 8\pi/D$ where D is the domain-length in the shear-layer normal direction. Perturbation modes with wavenumbers of 8, 4, 2, and 1 were chosen for the streamwise and spanwise directions. The dominant mode with wavenumber 8 was given a magnitude equal to ten percent of the half-domain height for the streamwise direction and a magnitude equal to five percent of the half-domain height for the spanwise direction. All other perturbations were randomly provided magnitudes of either three percent or one percent of the half-domain height. Phase shifts in the streamwise and spanwise direction were randomly chosen for this study. Density was initialized from the ideal gas law assuming constant pressure, identical free-stream density values for both shear-layer streams, and using the Crocco-Busseman relation for temperature

$$\rho = \rho_0 \left[1 + \frac{1}{2}\left(\gamma - 1\right) M^2 \left(1 - \tanh\left(\frac{\xi}{2\delta_\theta}\right)\right)\left(1 + \tanh\left(\frac{\xi}{2\delta_\theta}\right)\right)\right] \ . \tag{31}$$

Pressure was initialized assuming a constant pressure profile with correction for the velocity perturbations

$$p = p_0 - \frac{1}{2}\rho_0 \left(\hat{u}^2 + 2\hat{u}U_0 \tanh\left(\frac{\xi}{2\delta_\theta}\right) + v^2\right)\left(\gamma - 1\right) \ , \tag{32}$$

where $\hat{u}$ is given by

$$\hat{u} = u - U_0 \tanh\left(\frac{\xi}{2\delta_\theta}\right) \ . \tag{33}$$

The double-shear problem provides an anisotropic turbulent test case in which the turbulence is fed by a large-scale energy reservoir consisting of the freestream flow. This energy reservoir allows the problem to temporally evolve until the turbulence reaches the periodic boundaries, essentially mimicking a forced turbulence problem. At this point, the energy is able to decay away. Although it is a relatively simple problem configuration, the double-shear case provides a test of flow features commonly encountered in real-world engineering problems. The large-scale anisotropy is common in almost any wall-bounded or jet-type flow as is the continual production of turbulent energy from large-scale flow features that persist for long time-periods.

4.3 Simulations and Data Analysis

A non-dimensional, characteristic time, τ, is utilized for all the results presented. This "eddy turn-over" time is defined as

$$\tau = t\frac{U}{L} \ , \tag{34}$$

where U is the turbulent velocity and L is the integral length scale. The decaying Taylor-Green cases transition to fully developed turbulence by $\tau \approx 10$. After this point, the kinetic energy decays away due to the energy cascade process. The shear-layer spectrum transitions to fully developed turbulence by $\tau \approx 20$.

The results of interest in this study are presented using the three-dimensional kinetic energy spectra from each case. All spectral data is computed from instantaneous flow data.

5 Results and Discussion

5.1 Infinite Reynolds Number Taylor-Green Vortex

Results of the infinite Reynolds number Taylor-Green vortex case are presented in Figures 2 - 8. For convenience, the results are grouped into three categories: (1) the underlying FVMs, (2) the use of the PPM limiter in the underlying FVMs, and (3) the use of the SV SGS model. The underlying FVMs are second-, fourth-, and fifth-order accurate in their spatial discretization order of accuracy, respectively. Note that the PPM limiter is not implemented in the second-order scheme. Results presented in future sections will follow this format. For all of the tests, the unstabilized centered schemes displayed unbounded solution quantities and, as a result, are not included in any of the following figures.

As mentioned in section 4.3, spectral data presented throughout this study is computed from instantaneous simulation data. Figure 2 presents fourth-order SV results from a range of times. It is noted that the solution does not change dramatically over the course of $\Delta\tau = 0.4$ and time-averaged spectral results are unnecessary.

The results presented throughout this study do not use the SGS stress correction for the pressure computation of Eq. (10). Comparisons of inviscid Taylor-Green vortex simulations with and without the pressure correction showed no observable difference between the two in globally summed quantities and in energy spectra. For these low Mach number flows, this observation is expected.

As was also mentioned in section 4.3, the high-frequency information contained in the inviscid Taylor-Green vortex energy spectrum completely fills in by $\tau \approx 10$ as shown in Figure 3. After the high-frequency information is fully developed, the spectrum begins to decay away rather uniformly at the highest frequencies, while the lowest frequencies decay more rapidly. The straight, temporally self-similar form of the energy spectrum is expected to continue at higher mesh resolutions and later simulation times due to the lack of physical viscosity. As the simulation time progresses, the start of the constant-slope region is expected to push to higher and higher frequencies as more energy decays from the large scales into the smaller scales.

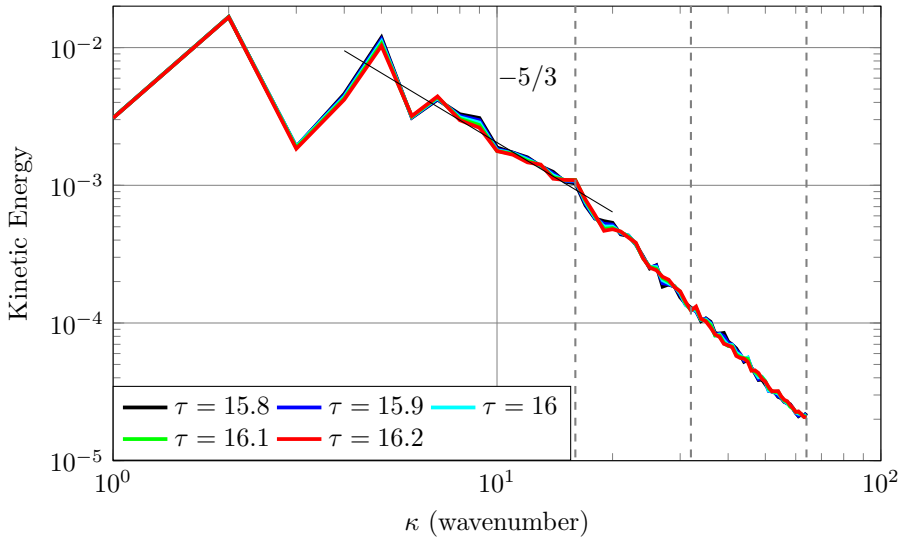

Fig. 2 Inviscid Taylor-Green vortex time evolution of kinetic energy spectrum over $\Delta\tau = 0.4$ from the fourth-order FVM with SV model on the 128^3 grid

The energy spectrum results obtained from all of the various algorithms tested in this study are presented in Figures 4 - 5. Focusing on the results obtained using the grid resolution of 128^3, it is apparent that when paired with the SV model, the centered schemes dissipate the highest frequencies significantly less than any other algorithm tested. Previous studies have noted the overly dissipative effects of upwind schemes on turbulence [18]. However, it is additionally noted here that, at 128^3 resolution, the strong small-scale dissipation provided by the upwind scheme distinctly alters the large-scale information over long time periods as compared with the centered schemes. In a high Reynolds number temporally-decaying turbulent flow, such as the test case under scrutiny, it is apparent that changes in near grid-cutoff scales can distinctly change the long-term evolution of apparently well-resolved scales. This change is attributed to the addition of the hyperviscosity-equivalent numerical dissipation associated with the upwind scheme. Merely adding the SV model to the fifth-order interpolation does not provide an improvement to the results unfortunately. In fact, the result is only more dissipative while retaining the same profile shape as the fifth-order results without the SV model.

Although the difference in large-scales between the centered schemes using the SV model and the upwind schemes is strongly apparent using a mesh size of 128^3, it must be noted that this is not the case for a mesh size of 512^3. In fact, the large scale information in both algorithms are extremely similar, even at late times ($\tau = 16$) as depicted in Figures 4 - 5. If high-frequency information is critical to the temporal evolution of the large-scales as is apparently the case here, it is suggested that upwind schemes should be avoided if possible.

While not quite as dissipative as the algorithms using upwinding, the fourth-order centered algorithm using the PPM limiter shows qualities similar to the

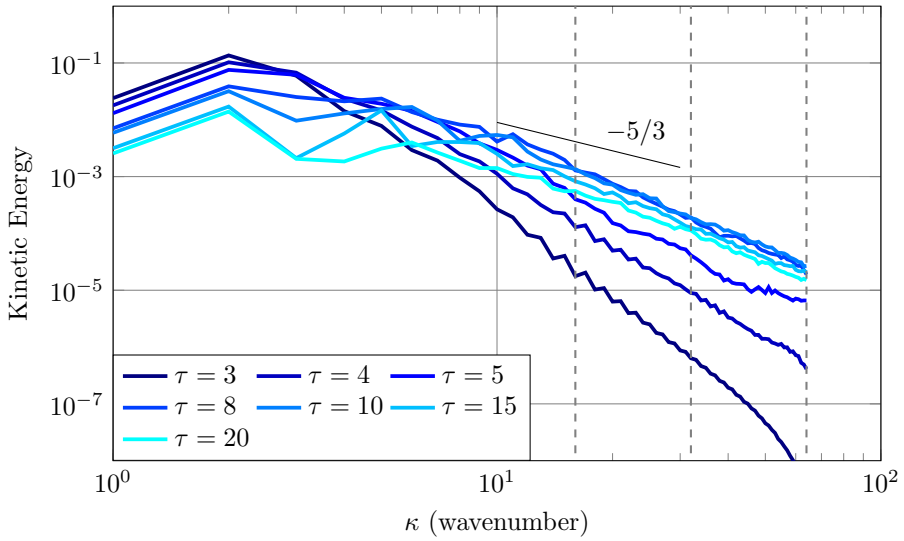

Fig. 3 Inviscid Taylor-Green vortex energy spectrum time-evolution from the fourth-order FVM with SV model on the 128^3 grid

fifth-order results in high wavenumbers. The long-time evolution of the large scales does not appear to be impacted by the limiter as much as it is in the case of the fifth-order scheme. The former provides more accuracy in high frequencies approaching to the $2\Delta x$ mode. If one were only interested in large-scale behavior, fourth-order PPM might be a viable candidate for ILES. However, if all wavenumbers are important, the limiter should be avoided or isolated to only act on true discontinuities. Even where necessary as in the case of a flow with shocks, isolating the limiter to only act on true discontinuities would be critical for successfully representing the energy spectrum at all wavenumbers.

As is visible in Figure 5 and more clearly seen in Figures 6 - 8, the SV model with the SGS vortex orientation vector aligned with $\mathbf{e^3}$ suffers from several deficiencies. Most notably, none of the scales show long-time grid-independence as the resolution increases. Early times show large-scale grid-independence as displayed in Figure 6. These early time periods also show an energy pileup at the grid-cutoff that becomes more prominent with increasing refinement. At later times as presented in Figures 7 - 8, increasing refinement leads to noticeable differences in large scales and more dissipation resulting in curved energy spectra near the grid-cutoff. Straight energy spectra would be expected due to the scale similarity of the inviscid Taylor-Green vortex. These results suggest that the orientation model using only $\mathbf{e^3}$ provides excessive dissipation and that a slightly less dissipative orientation vector may provide improved results.

Previous studies have demonstrated that the SGS vortex orientation model using resolved vorticity in addition to the strongest eigenvector of the strain-rate tensor is less dissipative than the model solely based on $\mathbf{e^3}$ [16, 21]. The results in Figures 4 - 8 bare this out as well. Early times of simulations using this model show even more pronounced energy pileup at the grid-cutoff than simulations using only

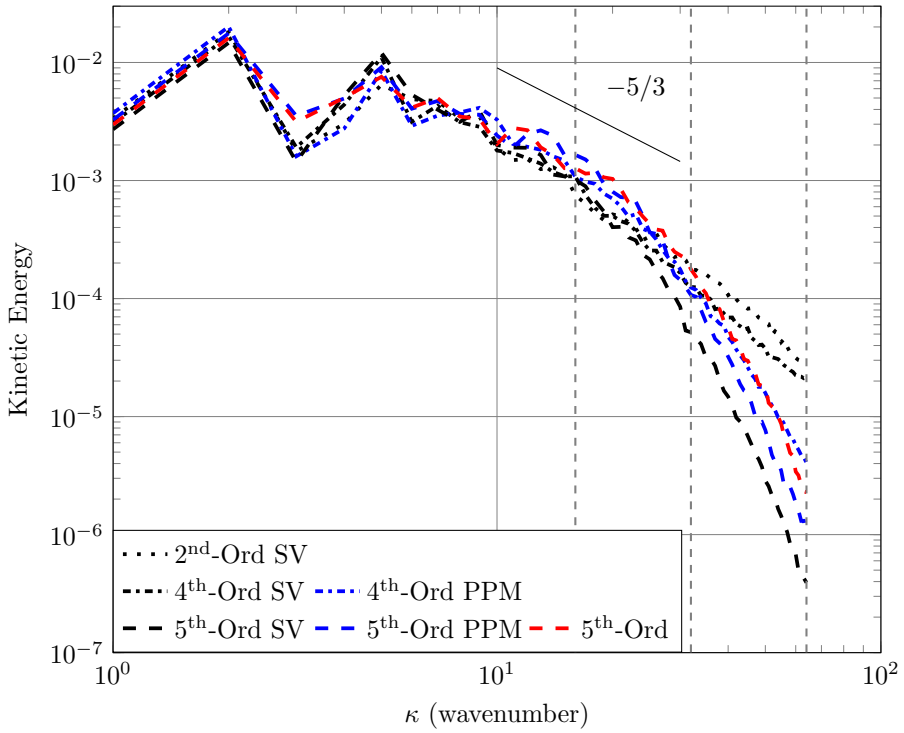

Fig. 4 Inviscid Taylor-Green vortex energy spectrum at $\tau = 16$

$\mathbf{e^3}$. While this may be undesirable should the magnitude of the energy pileup reach a sufficiently large value, turbulence is still developing during the early stages of the flow and the simulation remains stable. It may even be encouraging that the model isn't adding unnecessary dissipation during turbulence development. What is most encouraging regarding the second orientation model is the fact that the energy spectra display less variation as the resolution increases and large scales appear to be converging toward grid-independence at late simulation times. This study did not investigate the result of using other values of the σ weighting factor, but future simulations using this particular orientation model may benefit from such a parameter study.

5.2 Time Evolving Mixing Layer

The double-shear-layer results presented in this section will follow the same general format as the inviscid Taylor-Green vortex results and will consist of vorticity contours for demonstration of the flow evolution and three-dimensional kinetic energy spectra.

As shown in Figure 9, the double-shear-layer problem begins with the development of coherent vortices. These vortices rapidly break down and lead to full development of the kinetic energy spectrum by $\tau \approx 20$ as seen in Figure 10. The

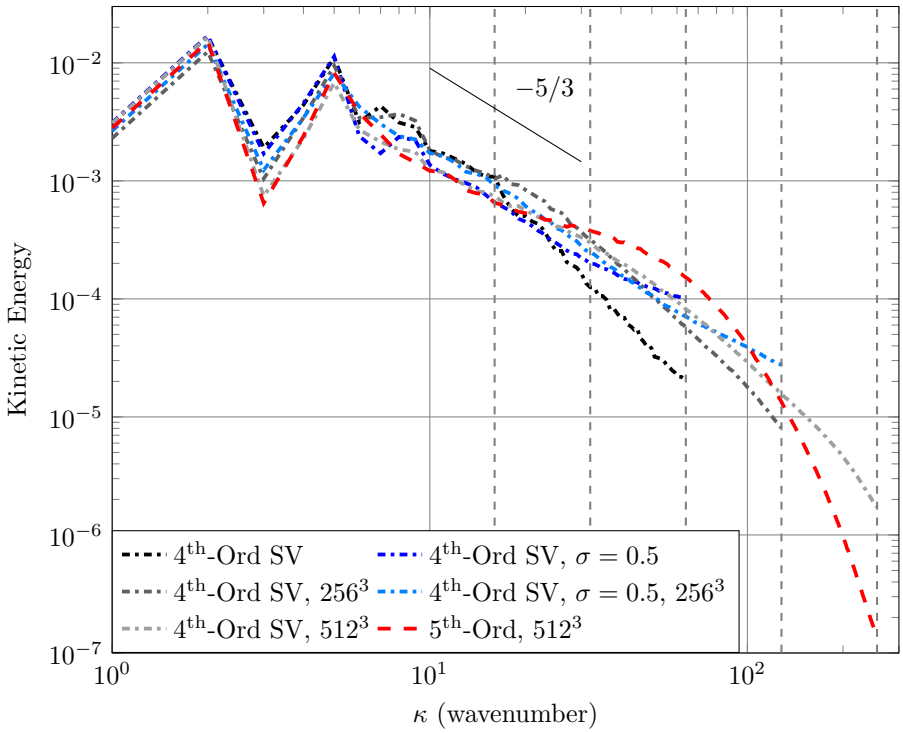

Fig. 5 Inviscid Taylor-Green vortex energy spectrum at $\tau = 16$

two layers continue to evolve in a turbulent manner and grow in the shear-layer normal direction until they begin interacting with one another at $\tau \approx 35$. Between $\tau \approx 20$ and at least $\tau \approx 80$, the kinetic energy spectrum is in a quasi-steady state, mimicking artificially forced turbulence quite well. This quasi-steady state allows for the study of the various algorithms in a distinctly different setting than the decaying Taylor-Green vortex problem.

Similar to the Taylor-Green results, results from the fifth-order upwind method both with and without the SV model as well as with the PPM scheme differ significantly from the centered-scheme results presented in Figure 11. Figure 12 shows that this persists throughout the entire simulation time and is not isolated to the smallest simulation scales. These results support the conclusion that the fifth-order scheme should be avoided in simulations of turbulent flows.

The fourth-order PPM results display an energy spectrum "hump" very similar to that display by the fifth-order results, but the largest scales are in closer agreement with all of the other centered-scheme results, indicating some degree of grid convergence. Furthermore, the $512 \times 512 \times 256$ fourth-order PPM case shows close agreement with the $128 \times 128 \times 64$ fourth-order SV and second-order SV results at large simulation scales. It is concluded that the SV model is able to accurately capture these scales using less resolution than is required by the fourth-order PPM scheme.

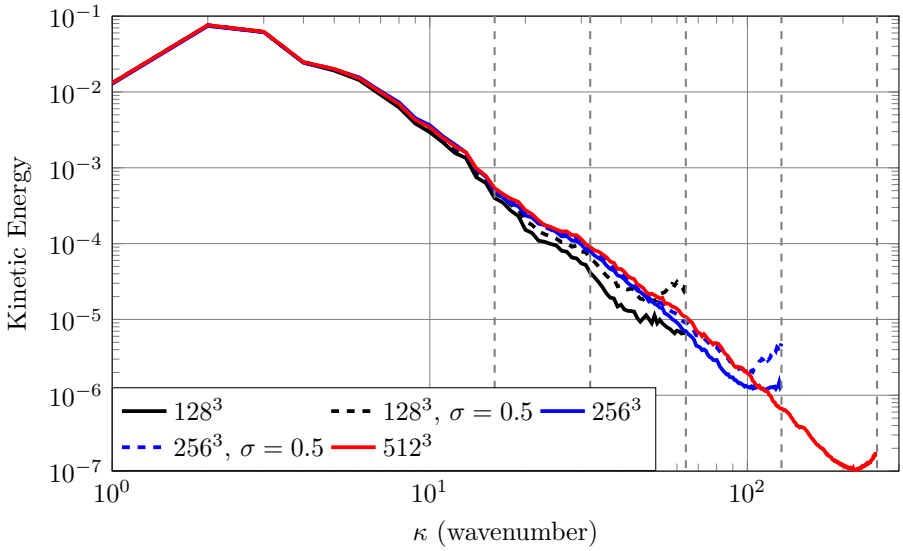

Fig. 6 Inviscid Taylor-Green vortex energy spectrum comparison using the fourth-order FVM with the SV model at $\tau = 5$

Examining the difference between the fourth-order and second-order methods using the SV model with the orientation model based on $\mathbf{e^3}$, it is apparent from Figure 11 and Figure 12 that the second-order algorithm shows significantly more time-variation, contrary to expectation of what should happen. While the fourth-order SV energy spectrum time-evolution is certainly more in line with expectation, it is difficult to say whether or not this is correct. However, the fourth-order SV results using only $\mathbf{e^3}$ appear to be best overall as they provide straight spectra all the way to the grid cutoff as is expected. Straighter spectra were obtained in the Taylor-Green results with a less dissipative SV model for the fourth-order schemes. As a result, it is likely that the difference in apparent dissipation at the highest frequencies between the second-order SV and fourth-order SV results is due to the decreased numerical dissipation associated with the fourth-order scheme.

The difference between the fourth-order SV orientation models is also quite distinctive and suggests that the orientation model based only on $\mathbf{e^3}$ is the appropriate model for this particular flow. In particular, the orientation model using $\sigma = 0.5$ shows as significant time-variation as the second-order SV results and produces spectra that are less straight than either of the fourth-order or second-order SV algorithms relying only on $\mathbf{e^3}$.

6 Conclusions

High Reynolds number, turbulent flows almost certainly require stabilization whether it be in the form of an explicit turbulence model, a limiter, or an upwind scheme for finite-volume methods. Low speed cases such as those investigated in this study

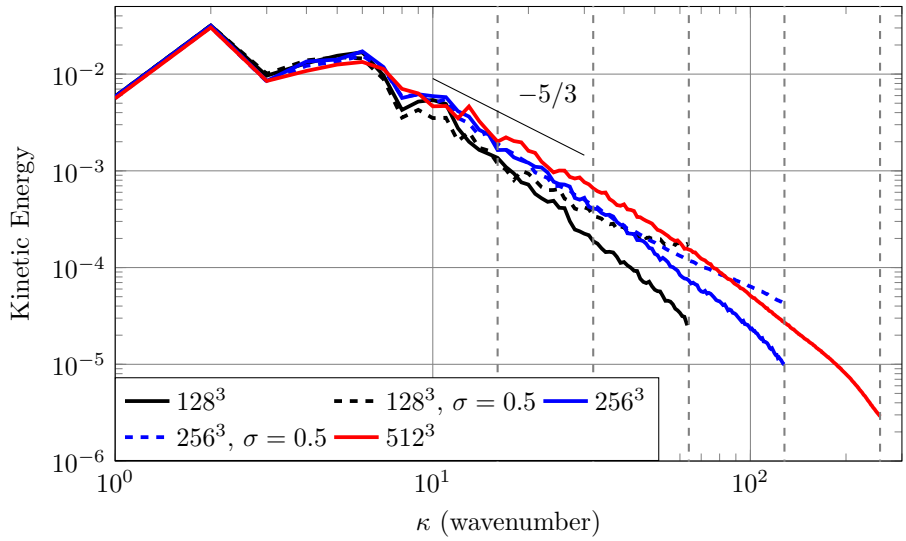

Fig. 7 Inviscid Taylor-Green vortex energy spectrum comparison using the fourth-order FVM with the SV model at $\tau = 10$

are best simulated using only the stretched-vortex explicit LES model. Both the PPM scheme and the fifth-order face-interpolation provide excessive dissipation at the highest frequencies and the resulting impact on the lowest frequency information is not ameliorated by adding the stretched-vortex model on top of the stabilization mechanisms already present. While the results obtained with only the SV model are sensitive to the SGS vortex orientation model utilized, the entire set of results using only SV model, taken as a whole, show more of a trend toward grid-independence than any of the results using PPM or the fifth-order interpolation.

In the context of fourth-order finite-volume methods, use of the standard SV model ($\sigma = 1$) provides the best overall prediction of spectrum for both cases. For the Taylor-Green vortex, there is evidence that a higher value of σ is more appropriate; however, this result might be specific to the Taylor-Green vortex or infinite Reynolds-number cases and introduces additional risk of instability in the code. If only the largest scales are of interest, a fourth-order stencil with PPM is the best candidate for ILES. The use of fifth-order upwinding negatively affects all scales and is not recommended.

For cases containing discontinuities, some form of interpolation limiting is required. Although the fifth-order interpolation effectively dampens the highest frequency content resolved by the mesh, it does so indiscriminately. The PPM scheme, on the other hand, only limits where it senses a discontinuity. As a result, it is plausible that the effects of the PPM limiter could be isolated to near-shock regions while the turbulent regions without shocks could remain free from limiting. The fifth-order interpolation could not achieve this and so should be avoided if at all possible. To localize the effects of the PPM limiter in the domain, future research will investigate the utility of applying an explicit filter to face-interpolated quan-

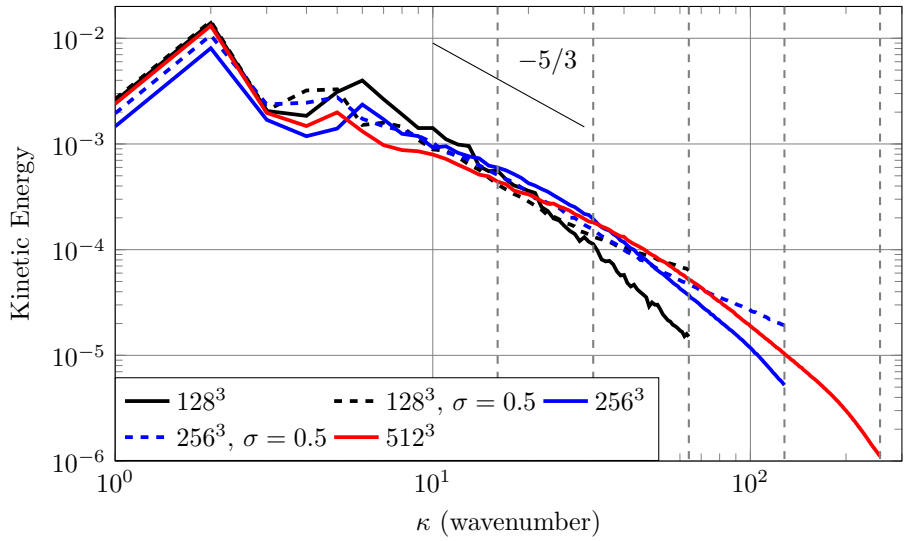

Fig. 8 Inviscid Taylor-Green vortex energy spectrum mesh comparison using the fourth-order FVM with the SV model at $\tau = 20$

ties before applying the limiter to the filtered field. Additionally, future research will further investigate the SGS vortex orientation model effects on various flows.

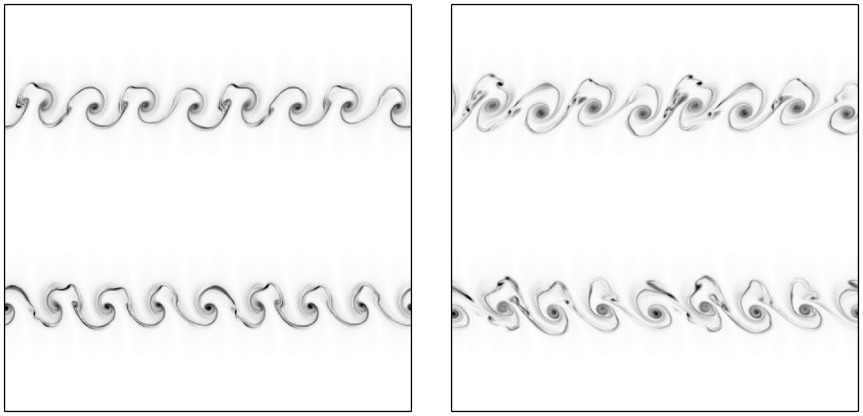

(a) $\tau = 2$

(b) $\tau = 3$

(c) $\tau = 5$

(d) $\tau = 10$

(e) $\tau = 20$

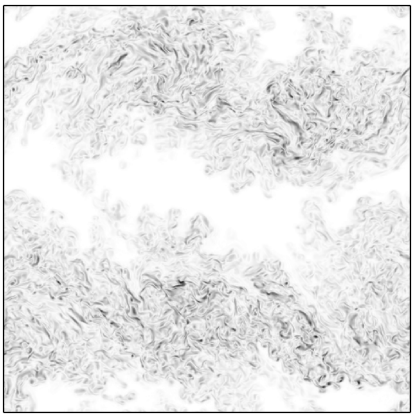

(f) $\tau = 50$

Fig. 9 Evolution of double-shear-layer vorticity magnitude from $\tau = 2$ to $\tau = 50$, mesh size $512 \times 512 \times 256$, fourth-order PPM algorithm. Increasing grayscale corresponds to increasing vorticity magnitude

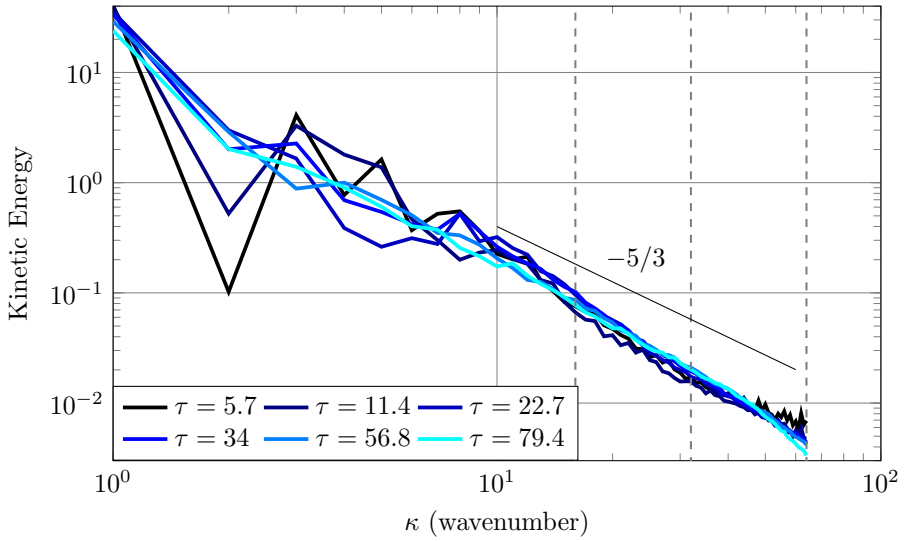

Fig. 10 Double-shear-layer time evolution of kinetic energy spectrum, fourth-order SV, $128 \times 128 \times 64$ mesh, shear-layer flow

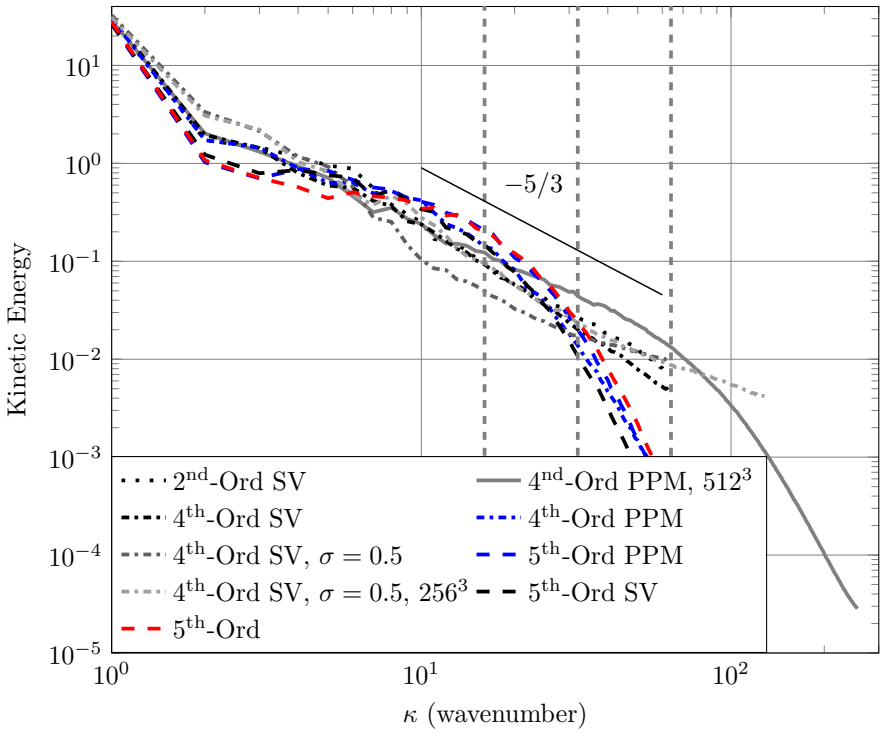

Fig. 11 Double-shear-layer energy spectrum at $\tau = 45.4$, $128 \times 128 \times 64$ mesh

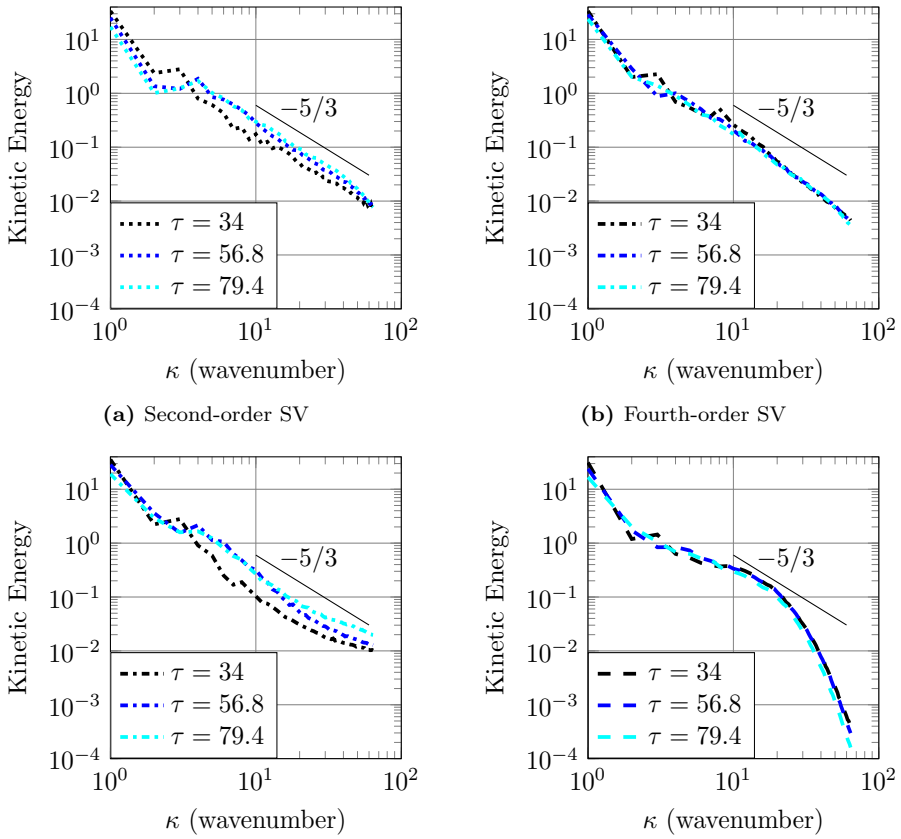

(a) Second-order SV

(b) Fourth-order SV

(c) Fourth-order SV, $\sigma = 0.5$

(d) Fifth-order

Fig. 12 Time evolution of energy spectrum for second-order SV, fourth-order SV, fourth-order SV with $\sigma = 0.5$, and fifth-order for the shear-layer flow

Conflict of interest

The authors declare that they have no conflict of interest.

References

1. Chung, D., Pullin, D.I.: Large-eddy simulation and wall modelling of turbulent channel flow. J. Fluid Mechanics **631**, 281–309 (2009)
2. Chung, D., Pullin, D.I.: Direct numerical simulation and large-eddy simulation of stationary buoyancy-driven turbulence. J. Fluid Mechanics **643**, 279–308 (2010)
3. Colella, P., Graves, D.T., Keen, N., Ligocki, T.J., Martin, D.F., McCorquodale, P., Modiano, D., Schwartz, P., Sternberg, T., Straalen, B.V.: Chombo Software Package for AMR Applications - Design Document. Lawrence Berkeley National Laboratory (2009). `https://seesar.lbl.gov/anag/chombo/ChomboDesign-3.0.pdf`
4. Colella, P., Sekora, M.: A limiter for PPM that preserves accuracy at smooth extrema. J. Comput. Phys. **227**(15), 7069–7076 (2008)
5. Gao, X., Guzik, S.M.J., Colella, P.: Fourth order boundary treatment for viscous fluxes on cartesian grid finite-volume methods. AIAA 2014-1277, 52nd AIAA Aerospace Sciences Meeting (2014)
6. Gao, X., Owen, L.D., Guzik, S.M.J.: A parallel adaptive numerical method with generalized curvilinear coordinate transformation for compressible Navier-Stokes equations. Int. J. Numer. Meth. Fluids **82**, 664–688 (2016)
7. Guzik, S.M., Gao, X., Olschanowsky, C.: A high-performance finite-volume algorithm for solving partial differential equations governing compressible viscous flows on structured grids. Comput. Math Appl. **72**, 2098–2118 (2016)
8. Guzik, S.M., Gao, X., Owen, L.D., McCorquodale, P., Colella, P.: A freestream-preserving fourth-order finite-volume method in mapped coordinates with adaptive-mesh refinement. Comput. Fluids **123**, 202–217 (2015)
9. Hill, D.J., Pantano, C., Pullin, D.I.: Large-eddy simulation and multi-scale modelling of a richtmyer-meshkov instability with reshock. J. Fluid Mech. **557**, 29–61 (2006)
10. Kosovic, B., Pullin, D.I., Samtaney, R.: Subgrid-scale modeling for large-eddy simulations of compressible turbulence. Phys. Fluids **14**(4), 1511–1522 (2002)
11. Lundgren, T.S.: Strained spiral vortex model for turbulent fine structure. Phys. Fluids **25**(12), 2193–2203 (1982)
12. Margolin, L.G.: Finite-scale equations for compressible fluid flow. Phil. Trans. R. Soc. A **367**, 2861–2871 (2009)
13. Mattner, T.W.: A refined stretched-vortex model for large-eddy simulation of turbulent mixing layers. Tech. rep., 17th Australasian Fluid Mechanics Conference (2010)
14. Mattner, T.W.: Large-eddy simulations of turbulent mixing layers using the stretched vortex model. J. Fluid Mechanics **671**, 507–534 (2011)
15. McCorquodale, P., Colella, P.: A high-order finite-volume method for conservation laws on locally refined grids. Comm. App. Math. Comput. Sci. **6**(1), 1–25 (2011)
16. Misra, A., Pullin, D.I.: A vortex-based subgrid stress model for large-eddy simulation. Phys. Fluids **9**(8), 2443–2454 (1997)
17. Owen, L.D., Guzik, S.M., Gao, X.: A high-order adaptive algorithm for multispecies gaseous flows on mapped domains. Comput. Fluids **170**, 249 – 260 (2018)
18. Sagaut, P.: Large Eddy Simulation for Incompressible Flows: An Introduction, 3rd edn. Springer-Verlag (1998)
19. Shetty, D.A., Frankel, S.H.: Assessment of stretched vortex subgrid-scale models for les of incompressible inhomogeneous turbulent flows. Int. J. Numer. Meth. Fluids **73**, 152–171 (2013)
20. Voelkl, T., Pullin, D.I., Chan, D.C.: A physical-space version of the stretched-vortex subgrid-stress model for large-eddy simulation. Phys. Fluids **12**(7), 1810–1825 (2000)
21. Walters, S., Guzik, S., Gao, X.: Evaluation of the stretched-vortex subgrid-scale model for large-eddy simulation with a fourth-order finite volume algorithm. In: 2019 AIAA SciTech Forum, AIAA 2019-1886. AIAA SciTech Forum (2019). https://doi.org/10.2514/6.2019-1886